

Full length article

Revisiting Precipitation kinetics in Mg-Zn alloy – a multi-characterization and modeling study

Yi Yang^a, Veronique Massardier^b, Mahmoud Reza Ghandehari Ferdowsi^a, Lu Jiang^a, Jun Wang^a, Thomas Dorin^{a,*}, Sitarama R. Kada^a, Matthew R. Barnett^a, Michel Perez^b

^a Institute for Frontier Materials, Deakin University, Geelong, VIC 3216, Australia

^b Université de Lyon, INSA-Lyon, MATEIS UMR CNRS 5510, 69621 Villeurbanne, France



ARTICLE INFO

Key words:

Magnesium alloy

Aging

Precipitation kinetics

Thermoelectric power

Modeling

ABSTRACT

This work aims to provide new insights into understanding precipitation kinetics in Mg-Zn alloys. First, the evolution of Zn solute, precipitate size and volume fraction is characterized using a combination of thermoelectric power, X-ray diffraction, atom probe tomography and transmission-electron microscopy in an Mg-1.7at.%Zn alloy when aged at 150 °C and 200 °C. The experimental results are then supported by a precipitation model based on classical nucleation and growth theories for rod and plate-shaped precipitates. It is found that rod-shaped precipitates are prevalent in the early aging stage, while plate-shaped precipitates dominate the over-aging stage. The kinetics of both precipitates are depicted in detail to represent this competition. Finally, a time-temperature-transformation diagram for these two types of precipitates is proposed for this system.

1. Introduction

Age hardening is a popular way to improve the mechanical properties of metallic alloys by introducing nano-scale precipitates to impede the movement of dislocations [1]. In Mg alloys, though the age hardening response is generally not as high as that seen in aluminium alloys, it is observed that the precipitates can increase or decrease the yield asymmetry, by influencing the twinning behaviour, based on their shape and size distributions [2]. Accurate characterization of size distribution and volume fraction with aging time is, therefore, essential to establish a structure-property relationship for future material development.

As one of the earliest age-hardenable Mg alloys developed [3], the Mg-Zn system has great potential in lightweight industrial design and degradable biomaterial applications due to its high specific strength, low corrosion potential and outstanding biocompatibility [4–7]. It is thus an important candidate for studying the precipitation in Mg alloys. The precipitation in Mg-Zn alloy begins with the formation of rod-shaped β_1 precipitates, followed by coarse plate β_2 precipitates, and reaches to the β equilibrium phase after a long aging time [8–11]. Both β_1 rods and β_2 plates have been reported to have strong hardening effects on slip and twinning [2,12–20]. In Mg-Zn alloys, it is generally accepted that the dominant strengthening phase is β_1 rods as the number

density of β_2 plates is usually low [12–19]. Understanding and optimising the distribution of these precipitates is key to maximise their impact on strength. The β_2 plates have been confirmed to display a hexagonal structure that is identical to the MgZn_2 phase. While the structure of the β_1 rods is in debate, it has been reported as either hexagonal MgZn_2 [21,22] or monoclinic Mg_4Zn_7 [23–26]. A recent study has observed that β_1 rods consist of a mixture of Mg_4Zn_7 and MgZn_2 phases for a cast Mg-3Zn alloy aged at 150 °C through a high-resolution transmission electron microscopy (TEM) investigation [27]. This information suggests that the β_1 phase experiences a structural transformation during aging or as a function of alloy composition.

Capturing the full formation kinetics of precipitates is known to be challenging. It involves characterising the evolution of various parameters as a function of time and temperature, including chemical and morphological information. Generally, if the types of precipitates are already known, measuring hardness evolution is the easiest and most popular way to indirectly follow the precipitation kinetics [1,8,21], but it does not provide any microstructural information. Transmission-electron microscopy (TEM) is particularly useful for measuring the morphological parameters of precipitates and is frequently applied in Al and Mg alloys [28–31]. Jain *et al.* [17] used TEM to study the precipitation kinetics in an Mg-6Zn alloy aged at 200 °C.

* Corresponding author.

E-mail address: thomas.dorin@deakin.edu.au (T. Dorin).

<https://doi.org/10.1016/j.actamat.2023.119276>

Received 1 May 2023; Received in revised form 1 August 2023; Accepted 19 August 2023

Available online 24 August 2023

1359-6454/© 2023 The Authors. Published by Elsevier Ltd on behalf of Acta Materialia Inc. This is an open access article under the CC BY license (<http://creativecommons.org/licenses/by/4.0/>).

Rosalie *et al.* [32] combined TEM and Small angle X-ray scattering (SAXS) to characterise the precipitation kinetics during aging at 150 °C in an Mg-8Zn alloy. The size and volume fraction of rod precipitates are quantitatively investigated in their work, but the authors report significant variations between their TEM and SAXS results. These variations can come from the small volume analyzed in TEM and large errors arising from the difficulty in correctly measuring the TEM foil thickness to obtain the precipitates volume fraction quantitatively. Atom probe tomography (APT) is also commonly used to assess precipitate morphology and compositions. A limited number of studies have used APT on Mg alloys [33–36]; for example, Honma *et al.* [35] detailedly analyzed the chemistry of nanoscale precipitates in an Mg-Gd-Y-Zr alloy aged at 200 °C using APT. In a recent study by Mo *et al.* [33], Gd-Ca co-clusters were verified for the first time through APT in a solution-treated Mg-Gd-Ca alloy responsible for the solid solution hardening. However, APT only analyzes a small volume and can lack statistical relevance compared to the bulk.

An alternative way to quantitatively analyze precipitation mechanisms is by using techniques sensitive to variations in solid solution, such as conductivity and Thermoelectric power (TEP) measurements. TEP measures the magnitude of an induced thermoelectric voltage in response to a temperature difference across a material. The TEP of alloys is strongly influenced by the presence of solute atoms; therefore, it is a sensitive tool to follow the precipitation kinetics [37,38]. The advantage of this technique is that it requires minimal sample preparation and data analysis while providing considerable accuracy and statistical information on a bulk sample. So far, TEP has been successfully applied to follow precipitation in a range of alloying systems such as steel, Al and Cu alloys [37,39,40], but it has yet to be applied to Mg alloys. Solute elements change not only electrical resistance, but also the lattice parameter, which can be measured by XRD [41,42]. Filep *et al.* [42] approximated the solid solution concentration in Al alloys by measuring lattice parameters through XRD, with the help of a known correlation between solute concentration and the change of lattice parameters. This method is an efficient way to test solute concentration and the influence from a second phase can be mostly avoided.

Accurate characterization of precipitation kinetics is paramount to building extensive databases that can be used to calibrate robust precipitation predictive models. Generally, precipitation models provide computed evolution of a wide range of parameters such as precipitate size, number density and volume fraction as a function of aging time and temperature. The commonly used mean-field approach [43–45] couples nucleation, growth and coarsening into a continuum level, usually based on KWN (Kampmann-Wagner-Numerical) model [43], and has been successfully operated in Al alloys and steel due to their efficiency and simplicity [46–51]. Although these models are often limited to simple cases such as spherical precipitates, efforts have been made to extend these models to the case of non-spherical precipitates. Robson [52] developed a coupled KWN model and successfully predicted the competition between continuous and discontinuous precipitation of plate-shaped precipitates in an AZ91 alloy. Bardel *et al.* [53] proposed a modified KWN model by introducing a shape factor $\xi = l/r_p$, where l is the precipitate length and r_p is the tip diameter, to successfully model the evolution of radius and volume fraction of needle-shaped precipitates in a 6061 alloy. A similar shape factor has been adopted by Chen *et al.* [54] to model the precipitation kinetics of needle-shaped precipitates in Al-Mg-Si alloys. In these cases, the precipitate aspect ratio is considered constant, and its value is found to influence the growth rate of precipitates. Holmedal *et al.* [55,56] successfully modelled the formation kinetics of needle-shaped precipitates in Al-Mg-Si alloys using a modified KWN model which incorporated an evolution of the precipitates' aspect ratio. This approach has also been adopted by Li *et al.* [57] to describe the precipitation kinetics of disk-shaped particles in Al alloys. Very recently, Miao *et al.* [58] modelled the precipitation in Mg-Al-Sn alloys using an improved KWN model combined with the Svoboda-Fischer-F-Kozeschnik (SFFK) model

where the changing aspect ratio of non-spherical precipitates has also been considered. While the changing aspect ratio provides better richness of describing precipitate shape evolution, it requires certain knowledge of crystallography of the precipitate/matrix interface and on the growth mechanism. Fixed aspect ratio is still commonly used for its efficiency [52–54,59], especially in some less studied alloying systems such as Mg-Zn alloys [59]. Paliwal *et al.* [60] and Robson *et al.* [59] proposed modified KWN models to study the evolution of rod-shaped precipitates in Mg-Zn alloys, the results have been compared with the experimental data from Jain *et al.* [17] and Rosalie *et al.* [32]. The proposed models roughly agree with experiments, but inconsistencies are still found between them. The asymmetrical nature of precipitates in Mg-Zn alloys and the complexity of precipitate compositions make it challenging to characterize and accurately describe precipitation kinetics in these alloys. The current work aims to improve the understanding of the precipitation process in Mg-Zn alloys required to develop meaningful and accurate precipitation kinetics models.

In this paper, we analyze the precipitation kinetics of rod and plate-shaped precipitates in an Mg-Zn alloy by using a combination of TEP, TEM, XRD and APT. TEM observation is conducted to measure the shape, size and distribution of rod and plate precipitates. TEP, XRD and APT are employed to characterize the solute evolution during aging. In addition, a modified KWN model for rod and plate-shaped precipitates is applied to support the experimental results by giving a detailed view from thermodynamics aspects. Here, for the first time, a combination of multi-characterization and modeling is used to follow the precipitation kinetics of β_1 and β_2 in a Mg-Zn alloy.

2. Materials and methods

2.1. Alloy preparation

The material used in this study is an extruded Mg-1.7at.%Zn alloy. The cast Mg-1.7at.%Zn was solution treated at 330 °C for 24 h and 370 °C for 120 h, followed by extrusion at 350 °C with a reduction ratio of ~36 and ram speed of 0.1 mm/s.

In order to consider the solute loss due to aging, reference alloys are obtained following the same procedures with Zn concentrations of ~0.7 at.% and ~1.1 at.%.

2.2. Isothermal aging

Two groups of samples were prepared for the aging treatment: raw extruded samples and samples solution treated after extrusion at 370 °C for 6 h and 12 h. Isothermal aging was then performed at 150 °C and 200 °C using a silicon oil bath; all samples were quenched in water at ambient temperature after aging. Note that the reference sample Mg-0.7at.%Zn and Mg-1.1at.%Zn followed the same solution treatment, then the Mg-0.7at.%Zn sample was aged at 150 °C and the Mg-1.1at.% Zn sample was aged at 200 °C for a long time. The PANDAT software was used to calculate the Zn content in the reference alloys. According to the phase diagram, the Zn contents of 0.7at.% and 1.1at.% correspond to the respective maximum solubilities of Zn in Mg at the aging temperatures of 150 °C and 200 °C after reaching equilibrium.

2.3. Hardness test

The hardness of samples with various aging conditions was measured using Vickers micro-hardness measurements and the surface of samples was mechanically polished up to 4000 SiC grit paper before testing. A load of 300 g and a holding time of 20 s were used for the measurements. The reported value is an average of at least 8 different indentations.

2.4. TEP measurement

Samples from all groups before and during the aging process were prepared for TEP measurement with a gauge size of 75 mm x 5 mm x 1.5 mm. TEP measures the voltage (V) arising from the Seebeck effect between the two junctions of studied material which are attached to a reference pure metal (here, pure Cu was used) [37]. During the measurements a temperature gradient (ΔT) at the junctions is established. In the current study, the temperature of the blocks used was T and T+ ΔT with T = 15 °C and ΔT = 10 °C. The relative TEP is defined as:

$$S = S^* - S_{Cu}^* = \Delta V / \Delta T \quad (1)$$

Where S^* is the absolute TEP of the studied alloy and S_{Cu}^* is the TEP of pure Cu.

The absolute TEP S^* of a Mg alloy is affected by the defects present in the Mg matrix and can be represented as:

$$S^* = S_{Mg}^* + \Delta S_{SS} + \Delta S_d + \Delta S_{pp} \quad (2)$$

Where S_{Mg}^* is the TEP of pure Mg without defects. ΔS_{SS} , ΔS_d and ΔS_{pp} are TEP values induced by solid solution (ss), dislocation (d) and precipitates (pp).

The contribution of solute element Zn (concentration $[Zn]_{at.\%}$) on TEP of pure Mg ΔS_{SS} is given by the Gorter–Nordheim law [61]:

$$\rho \Delta S_{SS} = (\rho_0 + \alpha_{Zn} [Zn]_{at.\%}) \Delta S_{SS} = \alpha_{Zn} S_{Zn} [Zn]_{at.\%} \quad (3)$$

Where ρ_0 is the resistivity of pure Mg, α_{Zn} is the specific resistivity of Zn in Mg (expressed in $\mu\Omega \cdot \text{cm} \cdot \text{at.\%}^{-1}$) and S_{Zn} is the specific thermoelectric power of Zn in Mg (in $\mu\text{V} \cdot \text{K}^{-1}$).

As far as precipitates are concerned, small coherent or semi-coherent precipitates are likely to have an intrinsic effect, depending on their shape, size and volume fraction. In contrast, the influence of large incoherent precipitates is negligible [37–40]. Dislocations can also have a minor influence on the TEP. For example, in Fe alloys, the increased dislocation density was shown to result in a decrease in the TEP [38]. In the current study, the precipitates are large enough so that their effect on the TEP will be minimal [37–40]. Assuming only solute atom variations influence TEP ($\Delta S_d = \Delta S_{pp} = 0$), the Gorter–Nordheim law can be applied to estimate the solute variations [61]:

$$\Delta S_{SS} = S^* - S_{Mg}^* = \frac{\alpha_{Zn} S_{Zn} [Zn]_{at.\%}}{\rho_0 + \alpha_{Zn} [Zn]_{at.\%}} \quad (4)$$

Where $S^* - S_{Mg}^*$ can be obtained by subtracting measured relative TEP of pure Mg from relative TEP of studied Mg alloy.

Eq. (4) can also be written as:

$$\frac{1}{\Delta S_{SS}} = \frac{A}{[Zn]_{at.\%}} + B, \quad A = \frac{\rho_0}{\alpha_{Zn} S_{Zn}}, \quad B = \frac{1}{S_{Zn}} \quad (5)$$

Where A and B are constant in this equation that can be determined by conducting a linear fit of $1/\Delta S_{SS}$ against $1/[Zn]_{at.\%}$.

2.5. TEM observation

Foils for TEM observation were machined from the center of aged samples with a thickness of 0.5 - 1 mm and manually ground to ~ 120 μm with 1200 grit SiC paper then to ~ 60 μm with 4000 SiC paper. 3 mm discs were punched from these thin foils using GATAN PIPS (precision ion polishing system) to make a hole through their center. The TEM observations were performed using a JEOL 2100 FEG TEM.

The size of rod and plate-shaped precipitates was measured by observing them perpendicular to the c-axis of the Mg matrix. To distinguish the overlapped particles, multiple TEM images with high magnification were taken and compounded together to cover a large area, and each condition is supported with at least 300 measured precipitates. The average aspect ratio is calculated from the measured

aspect ratio of all individual particles. The number density of precipitates was obtained by counting the number of particles in a specific area with known average thickness, where the foil thickness was estimated through the electron energy loss spectroscopy (EELS) technique with the assisted calibration from convergent beam electron diffraction (CBED) technique. The volume fraction of rod and plate-shaped precipitates was estimated by considering the average precipitate size and their number density.

2.6. Energy-dispersive X-ray (EDX) analysis

EDX analysis were carried out with a scanning electron microscope (SEM) to investigate the matrix solute distribution. Tests of plane parallel to the extrusion direction were performed using a field emission LEO 1530 SEM. Samples for EDX were grounded to 200, 600, 1200 grit, followed by polishing using colloidal diamond suspension. Finally, the samples were polished using colloidal silica solution. The accelerating voltage and working distance of each test were 20 kV and ~ 10 mm, respectively.

2.7. XRD measurement

X-ray diffraction measurements were carried out to quantify the concentration of solute elements in the Mg matrix. The measurements were performed in the powder diffraction beamline at the Australian synchrotron using a monochromatic beam of 21 keV (wavelength of 0.58998 Å) and with a spot size of $4 \times 1.2 \text{ mm}^2$ incident on the sample at 90° angle [62]. Samples of 1 mm thick were cut into thin pillars with the pillar's long axis along the extrusion direction. These pillars were rotated continuously to compensate for the orientation effects and to improve the grain sampling statistics. The diffraction profiles were analyzed using the TOPAS software suite [63] to evaluate the lattice parameters. The diffraction profiles were calibrated using a scan performed on Lanthanum-hexaboride (LaB6) sample using the same conditions as the sample.

2.8. APT measurement

APT samples were prepared by standard two-step electropolishing at room temperature. The APT experiments were carried out for samples peak aged at 150 °C and 200 °C using a Local Electrode Atom Probe (LEAP 5000XR) instrument (CAMECA Instrument, USA), operated in voltage mode at a pulse rate of 200 kHz and a pulse fraction of 20%. The temperature was controlled at 60 K and the detection rate was 0.5%. The APT data were reconstructed and analyzed using the CAMECA Integrated Visualization and Analysis Software (IVAS) version 3.8.2 software.

3. Results

3.1. Study of precipitation

3.1.1. Precipitation kinetics determined by TEP and hardness measurements

The relative TEP variations during aging of Mg-1.7at.%Zn were measured, samples were extruded and solutionized for 0 h, 6 h and 12 h at 370 °C followed by water quenching. In order to assess the homogeneity of solute and dislocations in the as-extruded sample (as this could impact the TEP signal), two groups of samples were cut from two different regions of the extruded material and marked as Extruded-A and Extruded-B. Fig. 1 shows the TEP variations (ΔS) of the extruded and solution-treated Mg-1.7at.%Zn alloy during isothermal aging at 150 °C (Fig. 1(a)) and at 200 °C (Fig. 1(b)), the variations are compared to the Vickers hardness kinetics of Mg-1.7at.%Zn alloy (Fig. 1(c) and (d)). The hardness and TEP are respectively found to increase and decrease during ageing up to peak hardness. After the peak hardness is reached, hardness

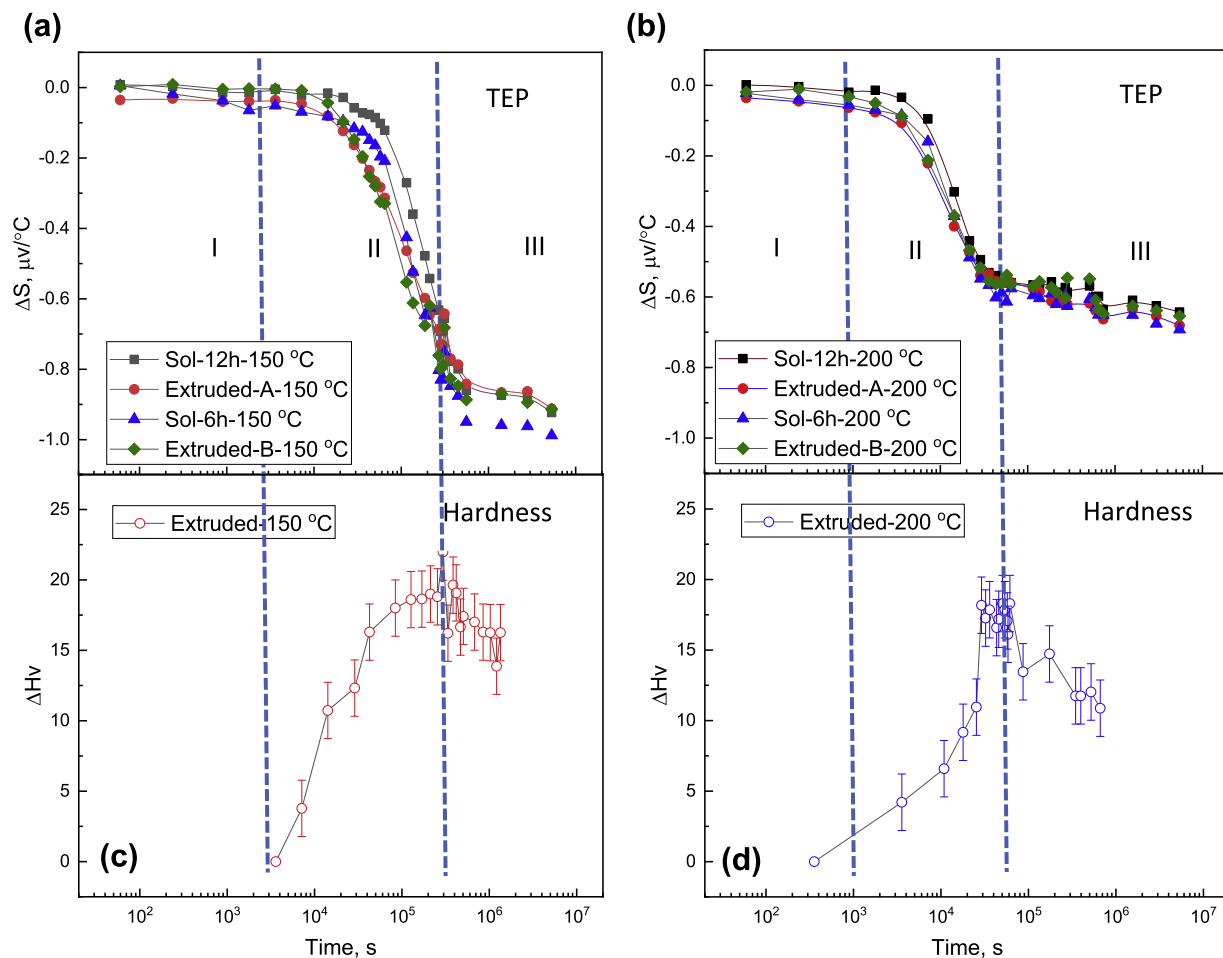


Fig. 1. comparison between TEP and hardness kinetics during aging at (a), (c) 150 °C and (b), (d) 200 °C. Extruded-A and Extruded-B are samples taken from different regions of the extruded material.

decreases which is a sign of precipitates' coarsening. The precipitation kinetics are found to be very similar in both as-extruded and as-solutionized samples, suggesting that the as-extruded samples are fully solutionized and the influence of dislocations on TEP results is negligible (Fig. 1(a) and (b)). For both temperatures, the TEP kinetics was found to be stable at the early stages of aging, followed by a sharp decrease, then the decreasing rate becomes slower and TEP seems to stabilise. Contrarily the hardness was found to increase and then to stabilise to a plateau before initiating a decrease over long aging times (Fig. 1(c) and (d)). Three distinct stages during aging can be identified from the kinetics: (I) The incubation time where both TEP variation and hardness increment are close to 0. (II) The growth stage where the TEP drops and the hardness increases. This stage corresponds to the precipitation of the rod-shaped β_1' phase, the dominant strengthening precipitate in the studied material [12,13,64]. Peak aging conditions are reached at the end of this stage, which is demonstrated by a plateauing of hardness increment at respectively ~ 20 ΔH_v and 17 ΔH_v at 150 °C and 200 °C. (III) During coarsening, the TEP decreases at a slower rate and the hardness starts to drop, indicating the over-aging of the alloy. The continued drop of TEP after peak aging indicates that the matrix solute content continues to drop, indicating that the precipitation process is still ongoing despite the drop in hardness, which is often largely attributed to coarsening. Three possible phenomena can be considered during this stage: 1. coarsening of the β_1' precipitates, which leads to the decrease of hardness and, 2. The formation of the β_2' precipitates, which leads to a decrease in solute concentration and a drop in TEP. 3. The decrease of solute concentration itself also leads to a decrease in

hardness. It is likely that the softening effects caused by coarsening of β_1' precipitates and loss of solute elements exceed the hardening effect from the formation of the β_2' precipitates. To further elucidate this, TEM is performed to characterize the precipitation at different aging stages in below section.

3.1.2. TEM characterization of precipitates during aging

The state of precipitation in the Mg-1.7at.%Zn alloy was observed at key aging times using TEM. Fig. 2 presents a selection of TEM images at peak aged conditions at 150 °C and 200 °C and over aged conditions at 200 °C. It is shown that, at all conditions, the dominant precipitate is β_1' along the [0001] axis. This is in agreement with the previous literature [12,13,64]. For peak aged conditions at 150 °C and 200 °C (Fig. 2(a) and (b)), the majority of precipitates observed are rod-shaped and a few blocky-shaped β_1' precipitates with no β_2' precipitates. The rod-shaped β_1' precipitates formed at the peak aging condition at 200 °C were observed to be shorter and thicker and with a smaller number density than that at 150 °C. When over aged at 200 °C (Fig. 2(c)), the presence of plate-shaped β_2' precipitates can also be observed.

The average size, number density and volume fraction of β_1' and β_2' precipitates obtained from TEM are summarized in Table 1 and Table 2. The size of both precipitates is increasing, and number density is decreasing with increasing aging temperature and time. The volume fraction of β_1' precipitates at 150 °C peak aging is twice larger than that at 200 °C peak aging, and the volume fractions of β_2' precipitates is negligible in the peak aged conditions. In the over-aged condition at 200

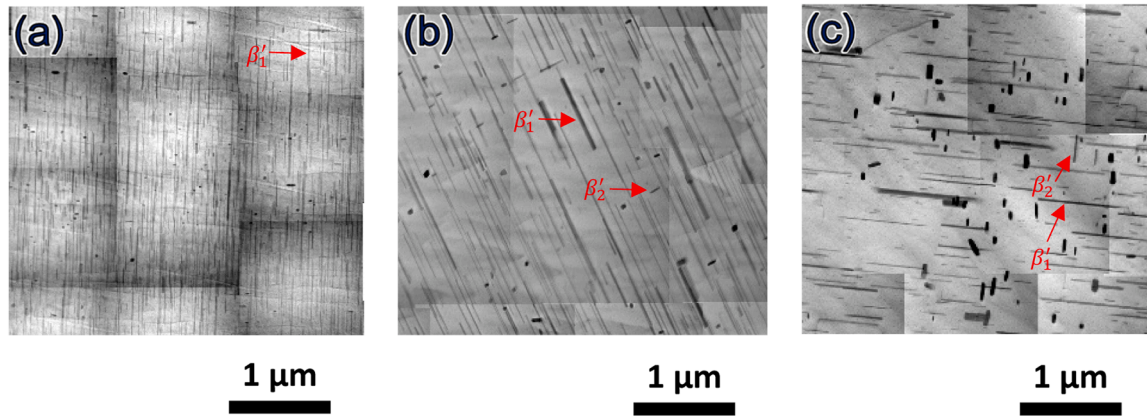


Fig. 2. TEM images of precipitates in aged Mg-1.7at.%Zn alloy. (a) aged at 150 °C for 84 h (peak aged). (b) aged at 200 °C for 12 h (peak aged). (c) aged at 200 °C for 180 h (overaged). In all figures, the zone axis is $[11\bar{2}0]$.

Table 1

Average size, number density and volume fraction of rod-shaped β'_1 precipitates calculated from TEM measurement at different aging conditions.

Aging conditions	Length l (nm)	Diameter r (nm)	Aspect ratio (l/r)	Number density (m^{-3})	Volume fraction
150 °C-84h (peak aging)	275 (± 10)	10(± 2)	29	4.3×10^{-20}	0.0093
200 °C-12h (peak aging)	395 (± 14)	11(± 3)	37	1.3×10^{-20}	0.0051
200 °C-180h (over aging)	251 (± 12)	19(± 8)	13	8.4×10^{-19}	0.0054

Table 2

Average size, number density and volume fraction of plate-shaped β'_2 precipitates calculated from TEM measurement at different aging conditions.

Aging conditions	Thickness t (nm)	Diameter r (nm)	Aspect ratio ($2r/t$)	Number density (m^{-3})	Volume fraction
150 °C-84h (peak aging)	13.9(± 0.4)	28.7 (± 1.4)	2.06	4.7×10^{-19}	0.00043
200 °C-12h (peak aging)	19.0(± 0.6)	50(± 2)	2.6	2×10^{-19}	0.00077
200 °C-180h (over aging)	39.3(± 1.4)	101.2 (± 3.4)	2.57	1.7×10^{-19}	0.0055

°C, the volume fractions of β'_1 and β'_2 precipitates appear to be similar. This is clear evidence that the β'_2 precipitates appear after peak aging and could be the main reason for the continued drop of TEP at stage (III) in Fig. 1. The volume fraction of β'_1 precipitates appears to plateau from peak aging to over aging at 200 °C combined with an increase of their diameter, showing a clear sign of coarsening. This also suggests that the β'_2 precipitates form as a new phase rather than arising from a structural transformation of the β'_1 precipitates.

3.1.3. APT measurement

To further analyze the state of precipitation in the peak-aged alloys, APT was used to analyze the matrix solute content in these conditions.

Fig. 3 (a) and (b) show the three-dimensional reconstructed volumes of alloys peak aged at 150 °C and 200 °C, respectively. The Mg and Zn solute are colored in grey and appear to be highly uniform in the collected APT volumes. Iso-concentration surfaces (colored in blue) were used to highlight the precipitates and to generate average proximity histograms for the two conditions, as shown in Fig. 3 (c) and (d). The presence of rod-shaped precipitates is revealed in the two studied volumes (Fig. 3 (a) and (b)) and the different precipitates are observed to be mostly aligned in the same direction, agreeing with the TEM results in Fig. 2. One precipitate in Fig. 3 (a) (colored in pink) is shown to have a slightly different orientation, compared to the other precipitates. This precipitate is possibly a part of the blocky-shaped β'_1 precipitate or an un-reported precipitate species. The proximity histograms in Fig. 3 (c) and (d) are computationally generated 1D composition profiles from the matrix to the center of the precipitates. The Zn content in the matrix was respectively found to be 0.59 and 0.72 at.% after peak aging at 150 °C and 200 °C. This increased matrix solute content as a function of temperature agrees with the increased Zn solubility when the temperature is increased.

The Zn-to-Mg ratio in the precipitates is found to be close to 3: 2 in the two samples, which differs from the commonly proposed ratio in the literature of $\sim 2: 1$. This difference might arise from the local magnification artifacts inherent to APT caused by the uneven evaporation rates of Mg (21 V/nm) and Zn (33 V/nm), which artificially enriches the precipitates with the matrix element. This points out the limits of using APT for obtaining accurate precipitate compositions. However, APT is a powerful tool to quantitatively assess the matrix solute content (far from the precipitate interfaces) that can provide a reliable tool to assess the state of the precipitation process.

3.2. Determination of the solute Zn content

3.2.1. Calibration of TEP and XRD

The Zn solute concentrations in aged alloys can be determined using TEP and XRD. However, the analysis of both TEP and XRD requires knowledge of the relationship between solute content and TEP signal/lattice parameter. This can be obtained from samples with known solute levels. To achieve this, solution-treated samples with Zn concentrations of ~ 0.7 at.%, ~ 1.1 at.%, and ~ 1.7 at.% were prepared and examined by EDX analysis. Relevant results are presented in Fig. 4. As can be seen, samples with ~ 0.7 at.% Zn and ~ 1.1 at.% Zn display a spatially homogeneous distribution of Zn, close to its nominal composition, while the sample with ~ 1.7 at.% Zn presents some local variations of Zn with concentrations between ~ 1.5 to 2 at.%. This is the result of micro-segregation during the casting of the alloys [65].

In addition, as revealed by the APT measurements conducted on the

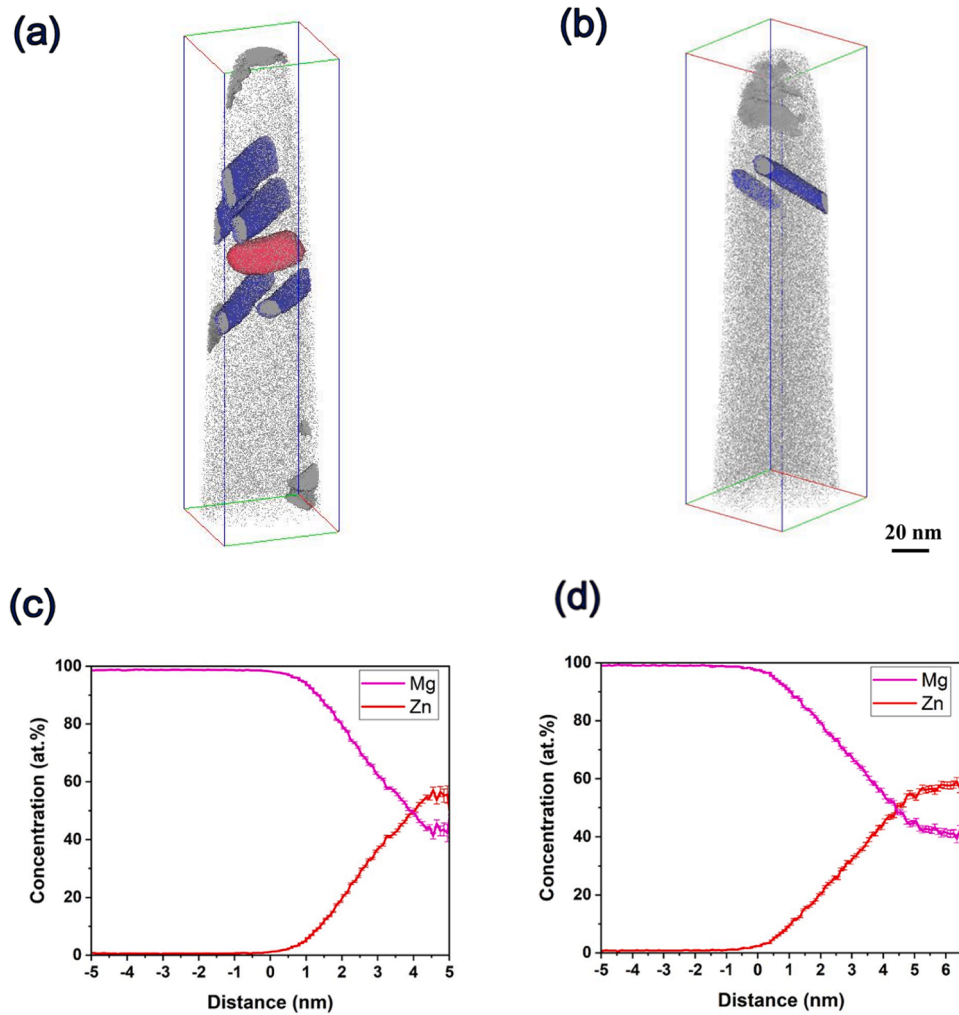


Fig. 3. Reconstructed elemental maps containing Mg and Zn of samples aged at (a) 150 °C for 84 h and (b) 200 °C for 12 h. Elements are colored in grey and iso-concentration surfaces are colored in blue to highlight the precipitates with the exception of one precipitate in (a) which shows different orientation with the other precipitates and is colored in pink. The corresponding proximity histograms of Zn iso-surface in (a) and (b) are presented in (c) and (d), respectively.

~ 1.7 at.% Zn sample (Fig. 5), Zn clusters are observed. The concentration of Zn solute content was found to be ~ 1.3 at.% in the analyzed volume. The small clusters are believed to be due to natural aging effects. Similar results were also reported in [9], where clusters are formed following the heat treatment of Mg-Zn alloys with higher Zn concentration. According to the EDX and APT results, distribution ranges of the element in the solution can be obtained for the three conditions.

As the bulk composition is known, $1/\Delta S_{SS}$ can be plotted against $1/[Zn]_{at. \%}$ in Fig. 6 after measuring the relative TEP of Mg-1.7at.%Zn, Mg-1.1at.%Zn, Mg-0.7at.%Zn alloys and pure Mg. The uncertainties in the composition measurements are obtained from EDX measurements, a 95% confidence band is presented to estimate the regression line between variables. The plots show a linear relationship, which validates the Gorter–Nordheim law in the current material. The constants A and B of Eq. (5) were calculated and the central relationship can be written in the following manner:

$$\frac{1}{\Delta S_{SS}} = \frac{0.4465(K * at. \% / \mu V)}{[Zn]_{at. \%}} + 0.3416(K / \mu V) \quad (6)$$

The lattice parameters measured from XRD in Mg-Zn with different additions of Zn in magnesium alloys are shown in Fig. 7. The trend is linear, which agrees with [66], and the central relationship for the three parameters are:

$$\text{For parameter } a: [a] = -0.0032 \left(\frac{\text{\AA}}{at. \%} \right) [Zn]_{at. \%} + 3.2088(\text{\AA}) \quad (7)$$

$$\text{For parameter } b: [b] = -0.0052 \left(\frac{\text{\AA}}{at. \%} \right) [Zn]_{at. \%} + 5.2101(\text{\AA}) \quad (8)$$

$$\text{For cell volume: } [cell \ volume] = -0.1396 \left(\frac{\text{\AA}^3}{at. \%} \right) [Zn]_{at. \%} + 46.4562(\text{\AA}^3) \quad (9)$$

This allowed us to determine the lattice parameters and, subsequently, the solute content in aged alloys.

3.2.2. Comparison between results from different techniques

Using the relationship in Fig. 6, the evolution of Zn solute as a function of aging time can be obtained from TEP and is compared to the solute obtained from other techniques in Fig. 8.

The lattice parameters of aged samples can be measured through XRD and their corresponding Zn concentrations can be derived using the linear relationships shown in Fig. 7, for each condition the result is the average of three parameters. The measured lattice parameters using XRD for aged alloys and the corresponding Zn concentrations are shown in Table 3.

The solute content from TEM is back-calculated from the measured

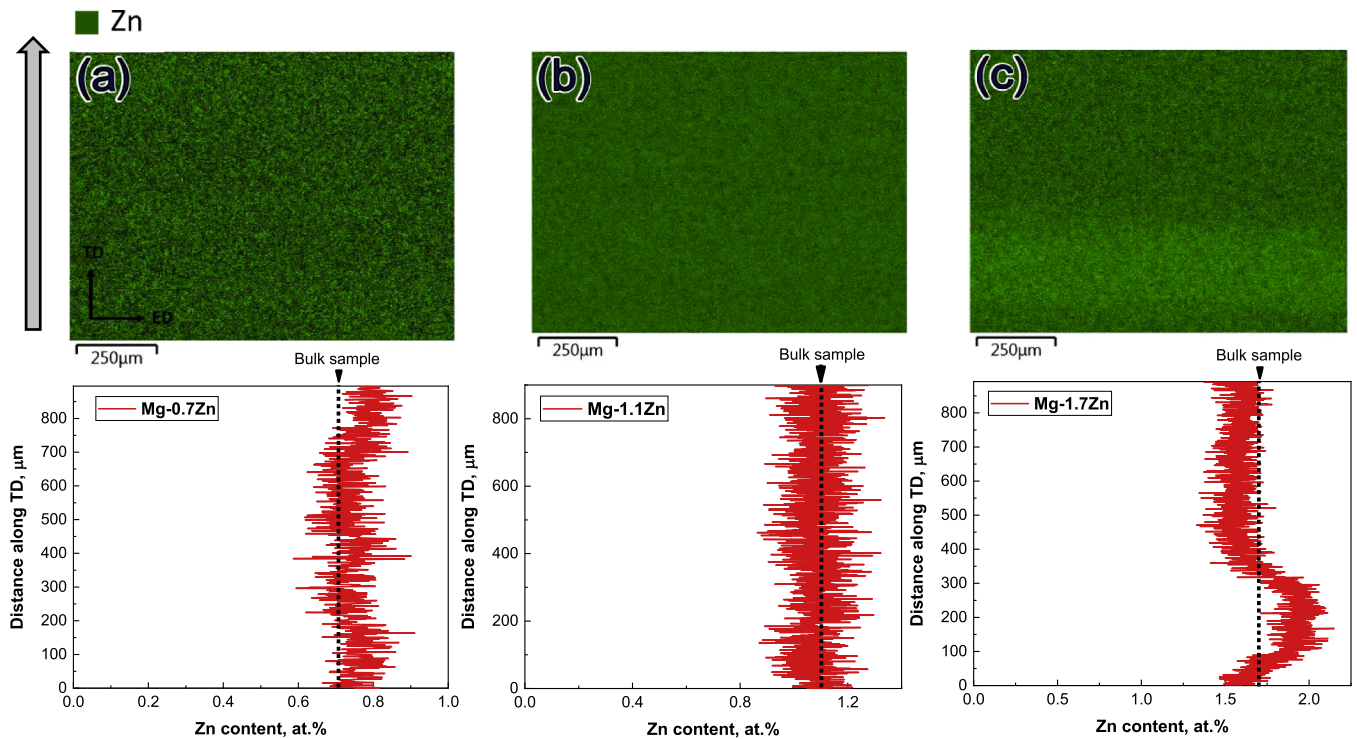


Fig. 4. EDX scans and relevant line scans along TD of samples solution treated for 6 h with Zn concentration of (a) ~ 0.7 at.%, (b) ~ 1.1 at.% and (c) ~ 1.7 at.%.

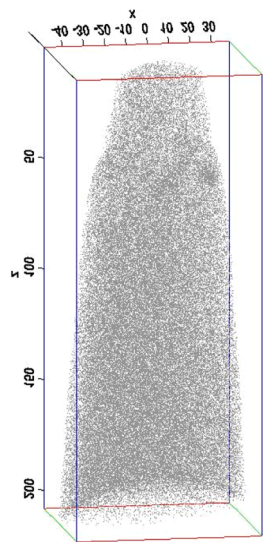


Fig. 5. Reconstructed elemental maps of Zn in an Mg-1.7at.%Zn sample solution treated for 6 h.

volume fractions of β_1^i and β_2^i precipitates using the equation below:

$$X_{Zn} = \frac{X_{Zn}^0 - \alpha X_{Zn}^p f_v}{1 - \alpha f_v} \quad (10)$$

Where f_v is the volume fraction of precipitates at each time step, α is the ratio of atomic volumes between Mg matrix and precipitates, X_{Zn}^0 is the initial atomic fraction of Zn in solid solution, here $X_{Zn}^0 = 0.0172$, X_{Zn} is the atomic fraction of Zn in solid solution at each time step, X_{Zn}^p is the atomic fraction of Zn in the precipitates. Here we assume the β_1^i precipitate composition is Mg_4Zn_7 , corresponding $X_{Zn}^p = 7/11$, and β_2^i precipitate composition is $MgZn_2$, corresponding $X_{Zn}^p = 2/3$. To address the atomic ratio α , the atomic volume of Mg, $MgZn_2$ and Mg_4Zn_7 are

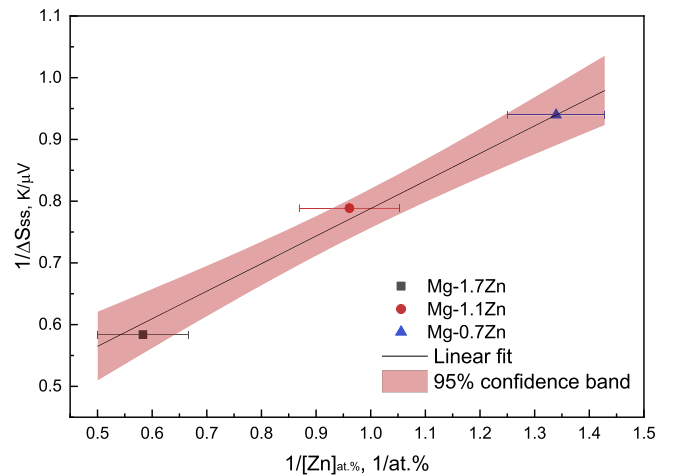


Fig. 6. Relationship between $1/[Zn]_{at. \%}$ and $1/\Delta S_{ss}$ derived from alloys with three different Zn concentrations.

calculated. For Mg, the atomic volume can be obtained through averaging volume by atom number in a lattice unit. The structure of $MgZn_2$ and Mg_4Zn_7 can be analyzed using the VESTA software [67], the atomic volumes of $MgZn_2$ and Mg_4Zn_7 are calculated as 1.62×10^{-29} and $1.72 \times 10^{-29} \text{ m}^3$. The atomic ratios α for $MgZn_2$ and Mg_4Zn_7 are then determined as 1.43 and 1.35.

Fig. 8 shows an overall agreement between the different techniques used to obtain solute content, particularly at long aging times. Larger discrepancies can be observed at intermediate aging times, which can be attributed to the uncertainties arising from the different techniques; this will be discussed in a later section.

It is also interesting to find that the solute limit from all techniques in the current study ($\sim 0.5 - 0.6$ at.% at 150°C and $\sim 0.7 - 0.9$ at.% at 200°C) is lower than the equilibrium limit in Mg-Zn phase diagram from many popular databases such as KNOVEL (ASM Handbook, Volume 03 -

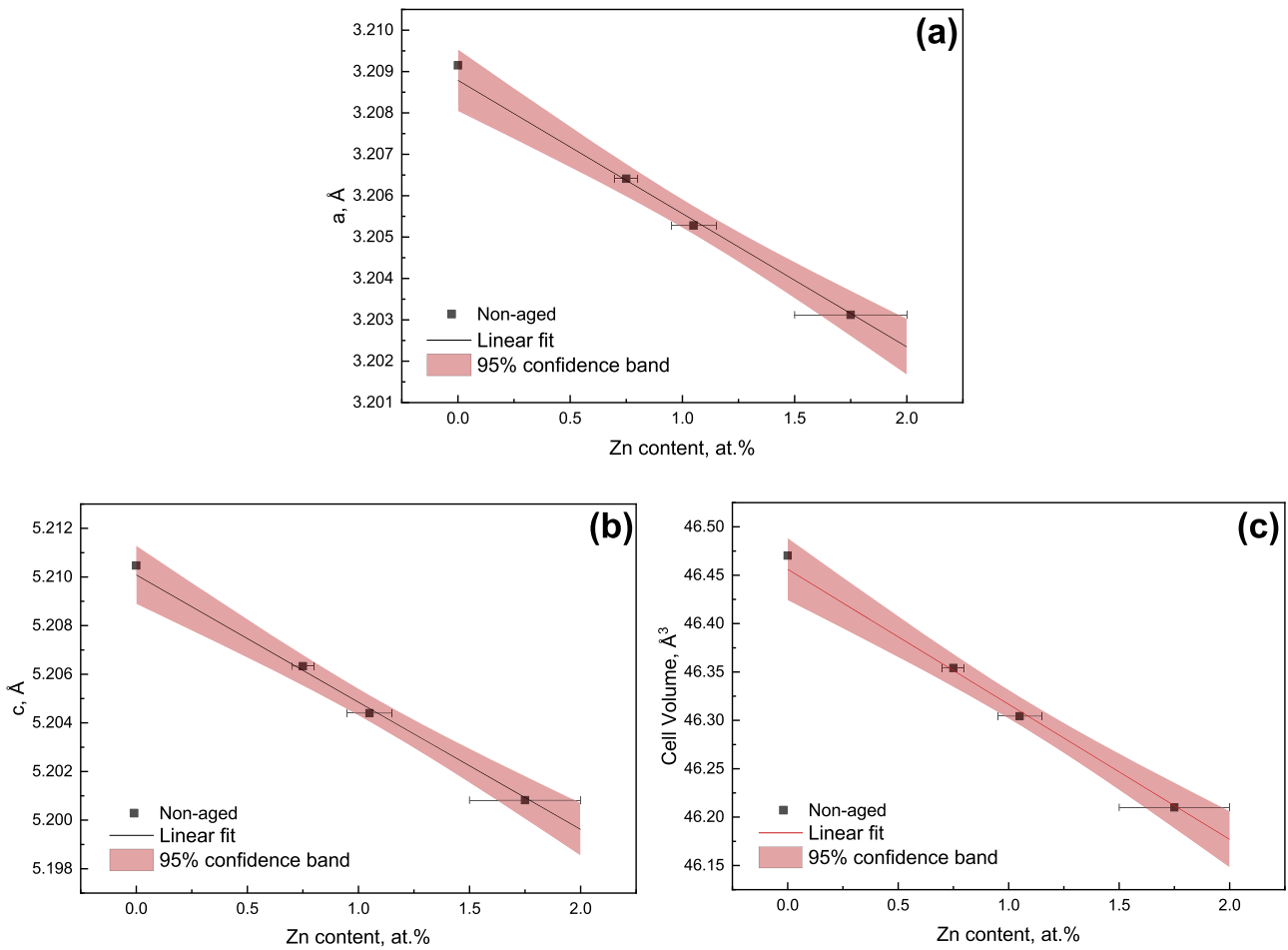


Fig. 7. Influence of the Zn content in Mg-Zn alloys on lattice parameters (a) a in Å, (b) c in Å and (c) the cell volume in Å³. Error bars are derived from Fig. 4.

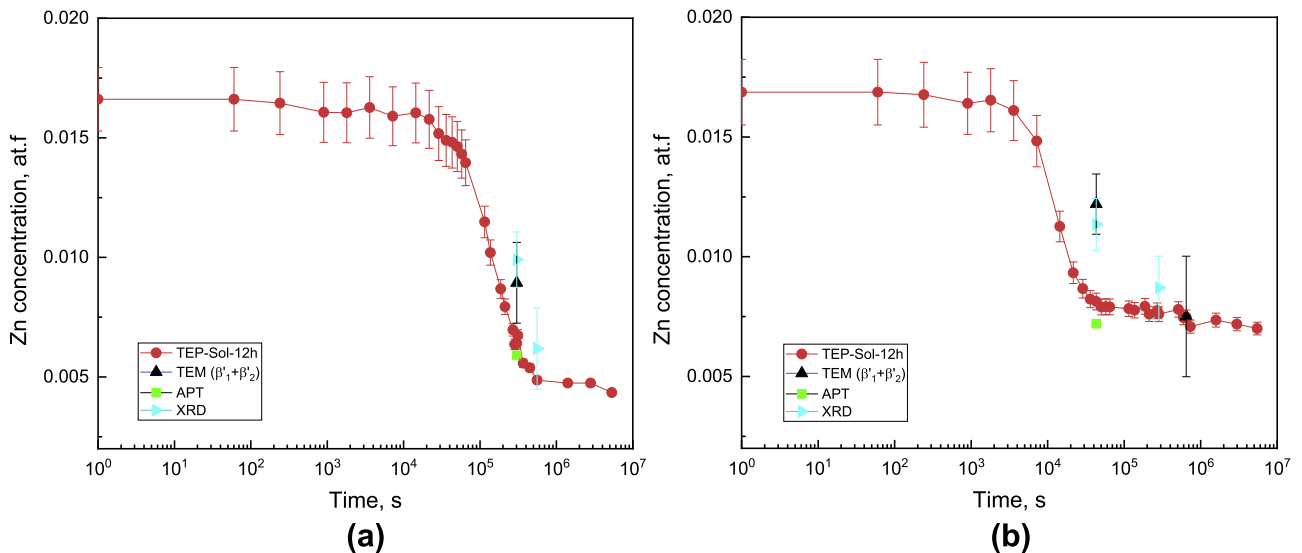


Fig. 8. Zn solute content at the different aging times obtained from different characterization techniques at (a) 150 °C and (b) 200 °C.

Alloy Phase Diagrams) [68] (~ 1.0 at.% at 150 °C and ~ 1.3 at.% at 200 °C), THERMOCALC (TT Mg-alloys database v4.2) [69] (~ 0.7 at.% at 150 °C and ~ 1.2 at.% at 200 °C) and PANDAT [70] (~ 0.7 at.% at 150 °C and ~ 1.1 at.% at 200 °C). The values in the mainstream database are calculated based on thermodynamic equations with specific parameters fitted from experiments in literature; thus, results are always slightly

different from database to database depending on their sources. The current study indicates that more work needs to be done to improve the phase diagram calculation.

Table 3

Measured lattice parameters and derived Zn concentration for alloys with different aging conditions using the relationships from Fig. 7.

Aging conditions	Measured a, Å (corresponding Zn concentration, at.%)	Measured c, Å (corresponding Zn concentration, at.%)	Measured cell volume, Å ³ (corresponding Zn concentration, at.%)	Derived Zn concentration, at.%
150 °C-84h (peak aging)	3.2057 (0.95±0.11)	5.2046 (1.03±0.11)	46.3191 (0.98±0.11)	0.99±0.11
150 °C-155h (over aging)	3.2068 (0.59±0.17)	5.2066 (0.65±0.16)	46.3707 (0.61±0.16)	0.61±0.17
200 °C-12h (peak aging)	3.2051 (1.13±0.1)	5.2041 (1.13±0.1)	46.2977 (1.13±0.1)	1.13±0.1
200 °C-180h (over aging)	3.2059 (0.87±0.13)	5.2055 (0.86±0.12)	46.3346 (0.87±0.12)	0.86±0.13

4. Precipitation modeling

Precipitation modeling was employed to analyze the formation kinetics of β'_1 and β'_2 precipitates. To distinguish the two precipitate species, all β'_1 rods are assumed to have a composition of Mg₄Zn₇, and β'_2 plates are assumed to have a composition of MgZn₂. This work is built on the PreciSo software [44,45]; it uses classical nucleation, growth, and coarsening theories which provides a prediction of precipitation kinetics during various heating process and is fully described in [43]. The precipitation state was characterized by a precipitation model tailored for rod and plate-shaped precipitates in the Mg-Zn system and the strategy is based on the precipitation model proposed by Perez *et al.* [44,45], and modified by Bardel *et al.* [53] and Balan *et al.* [71], which is briefly revisited below.

4.1. Precipitation model of rod and plate-shaped precipitates

The current model uses “a mean field multi-class approach” (Lagrange-like approach), which is based on the following assumptions:

- The nucleation is homogeneous and elastic energy is assumed to be negligible.
- The interfacial energy and chemical composition of precipitates are considered constant and do not vary with precipitate size, time or temperature.
- The rod-shaped precipitates are assumed to be equivalent to a cylinder of length $l - 2r_r$ and radius r_r , and the plate-shaped precipitates are assumed as plates of thickness h and radius r_p (see Fig. 9).
- The shape factors for rods $b_r = l/r_r$ and plates $b_p = 2r_p/h$ are considered constant as determined by the average value from TEM.

The classical nucleation theory represents the competition between volume energy and surface energy, and the total Gibbs energy change ΔG with the presence of rod and plate-shaped precipitates can be written as:

For rod [53]:

$$\Delta G = \left(b_r - \frac{2}{3}\right)\pi r_r^3 \Delta g + b_r 2\pi r_r^2 \gamma \quad (11)$$

For plate [71]:



$$\Delta G = \frac{2}{b_p} \pi r_p^3 \Delta g + \left(1 + \frac{2}{b_p}\right) 2\pi r_p^2 \gamma \quad (12)$$

Where Δg is the chemical driving force (has a negative contribution) and γ is the surface energy.

The critical radius r_r^* can then be modified as:

For rod [53]:

$$r_r^* = -\frac{2\gamma}{\Delta g} \frac{2b_r}{3b_r - 2} \quad (13)$$

For plate [71]:

$$r_p^* = -\frac{2\gamma}{\Delta g} \frac{b_p + 2}{3} \quad (14)$$

So the energy barrier for nucleation becomes:

For rod [53]:

$$\Delta G^* = \frac{16}{3} \pi \frac{\gamma^3}{\Delta g^2} \frac{2b_r^3}{(3b_r - 2)^2} \quad (15)$$

For plate [71]:

$$\Delta G^* = \frac{16}{3} \pi \frac{\gamma^3}{\Delta g^2} \frac{(b_p + 2)^3}{18b_p} \quad (16)$$

The classical nucleation rate for rod and plate-shaped precipitates is given by [44,45]:

$$\frac{dN}{dt} = N_0 Z \beta^* \exp\left[-\frac{\Delta G^*}{k_b T}\right] \left[1 - \exp\left(-\frac{t}{\tau}\right)\right] \quad (17)$$

Where t is the aging time, τ is the incubation time, T is the temperature (in kelvin), k_b is the Boltzmann constant, N_0 is the nucleation site density, the current study considers homogeneous nucleation where every atom of the matrix is a possible nucleation site, then $N_0 = \frac{1}{v_{at}^m}$, where v_{at}^m is the atomic volume of the matrix. β^* is the condensation rate and Z is the Zeldovich factor. For rod precipitates, Z and β^* are given by [53]:

$$Z = \frac{v_{at}^p}{\pi r_r^{*2} (3b_r - 2)} \sqrt{\frac{2b_r \gamma}{k_b T}} \quad (18)$$

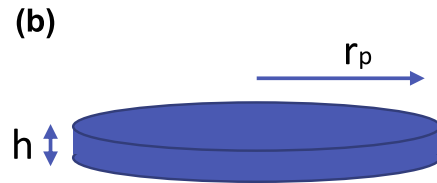


Fig. 9. Schematic illustration of (a) rod precipitate and (b) plate precipitate in the precipitation model.

$$\beta^* = \frac{4\pi r_r^{*2}}{a^4} \left(\frac{X_{Zn}^p}{D_{Zn} X_{Zn}} \right) \quad (19)$$

For plate precipitates, they are [71]:

$$Z = \frac{v_{at}^p}{3\pi r_p^{*2}} \sqrt{\frac{(b_p^2 + 2b_p)\gamma}{2k_b T}} \quad (20)$$

$$\beta^* = \frac{4\pi r_p^{*2}}{a^4} \left(\frac{X_{Zn}^p}{D_{Zn} X_{Zn}} \right) \quad (21)$$

Where v_{at}^p is the atomic volume of precipitate, a is the lattice parameter, D_{Zn} is the Zn diffusion coefficient. D_{Zn} can be expressed as [44,45]:

$$D_{Zn} = D_{Zn}^0 \exp\left[-\frac{Q_{Zn}}{RT}\right] \quad (22)$$

D_{Zn}^0 is the pre-exponential factor, Q_{Zn} is the activation energy of Zn, R is the gas constant.

The growth equation is using Zener-Hillert expression adapted for rod and plate-shaped precipitates:

For rod [53]:

$$\frac{dl}{dt} = 1.5 \frac{D_{Zn}}{2r_r} \frac{X_{Zn} - X_{Zn}^i}{\alpha X_{Zn}^p - X_{Zn}^i} \quad (23)$$

For plate [71]:

$$\frac{dl}{dt} = 0.5b_p \frac{D_{Zn}}{r_p} \frac{X_{Zn} - X_{Zn}^i}{\alpha X_{Zn}^p - X_{Zn}^i} \quad (24)$$

Where X_{Zn}^i is Zn atomic fraction at the interface.

The multiplicative term $1 - r^*/r$ in the original Zener-Hillert expression, which accounts for capillarity effects, is removed here because the Gibbs-Thomson effect is more efficiently accounted for in the current model [53,72].

The solubility product of precipitates is expressed in a classical form:

$$\log_{10} K_S = -\frac{A}{T} + B \quad (25)$$

Where A and B are parameters that need to be evaluated from experimental solubility limit.

At each time step, K_S for the precipitate with composition Mg_xZn_y is evaluated as:

$$K_S = X_{Mg}^x X_{Zn}^y \quad (26)$$

Finally, the mass balance is calculated to update the solute content as precipitation proceeds; it can be expressed as in Eq. (10). And f_i can be easily calculated by knowing the radius and number density of all modeling classes i .

4.2. Calibration of precipitation model

The precipitate solubility (A and B in Eq. (25)) can be acquired through a linear fitting of $\log_{10} K_S$ with $1/T$, by taking the K_S at 150 °C and 200 °C when the solute reaches equilibrium for certain precipitates. Here we estimate the solutes at peak aging conditions are the equilibrium for β_1 since β_1 rod is the dominant phase at this stage (Fig. 2), and we took the longest aging time (~ 2 months) for the equilibrium of β_2 as this is the condition where the largest amount of β_2 has formed. The Zn concentrations for calibration were obtained from APT and TEP and are corrected by the Gibbs-Thomson equation to eliminate the surface effect [72]:

$$[Zn]_{at.\%}^{GT} = [Zn]_{at.\%} \exp\left[-\frac{r_0^i}{r}\right] \quad (27)$$

For β_1 rod-shaped precipitates with composition Mg_4Zn_7 :

$$r_0^1 = \frac{4b_r \gamma_{at}^{\beta_1} \times (4 + 7)}{k_b T (3b_r - 2)} \quad (28)$$

For β_2 plate-shaped precipitates with composition $MgZn_2$:

$$r_0^2 = \frac{2(b_p + 2)\gamma_{at}^{\beta_2} \times (1 + 2)}{3k_b T} \quad (29)$$

Since in Eq. (19) and (21), only one lattice parameter is permitted while Mg alloy has two lattice parameters, the equivalent cubic structure with the same volume is considered, and an equivalent lattice parameter a is used. The diffusion coefficient for Zn has been taken from ref. [73]. The chemical composition of respectively rod-shaped β_1 and plate-shaped β_2 is assumed to be Mg_4Zn_7 and $MgZn_2$. Their atomic volume was calculated with VESTA [67]. The surface energy of precipitates was set as a fitting parameter.

Parameters for the precipitation model are listed in Table 4.

4.3. Simulation results

The simulated precipitate radius and number density in comparison with TEM results at 150 °C and 200 °C are presented in Fig. 10. The model is in reasonable agreement with the TEM results apart from the radius for β_1 rods (Fig. 10 (a)) for which the predictions are smaller than the radius directly measured from TEM, this discrepancy could come from the fixed aspect ratio and low surface energy used in the model. The radius of the β_2 plates is always higher than that of β_1 rods (Fig. 10 (a) and (b)); the β_1 rods start dissolving after peak aging where β_2 plates start coarsening, which is in good agreement with the TEM results. The number density of β_2 plates, on the other hand, has slower kinetics and is always lower than β_1 rods until β_1 rods dissolve (Fig. 10 (c) and (d)). Overall the current model and parameters give reasonable prediction of the precipitation kinetics of the studied alloy.

5. Discussion

5.1. Limitations of characterization techniques

The solute content at different aging conditions and the precipitation kinetics are compared in Fig. 8 using various techniques. Though the overall results show good agreement with each other, some differences are still observed at intermediate aging times.

The analysis of TEP and XRD has the advantage of measuring bulk volumes. However, both rely on the assumption that the initial solute composition is known. The solute contents obtained from TEP and XRD measurements also assume no contribution from the precipitates.

Table 4
Model parameters.

Parameters	β_1 (Mg_4Zn_7)	β_2 ($MgZn_2$)	Reference
X_{Zn}^0 (at%)	1.72	1.72	This work
X_{Zn}^p	7/11	2/3	
Aspect ratio	25 (b_r)	2.5 (b_p)	TEM
A	3759	1095	Derive from APT and TEP
B	-6.89	-2.06	
D_{Zn}^0 (m^2/s)	2.9×10^{-5}	2.9×10^{-5}	[73]
Q_{Zn} (kJ/mol)	118.6×10^3	118.6×10^3	[73]
γ (J/ m^2)	0.041	0.0753	fitted
v_{at}^p (m^3)	1.72×10^{-29}	1.62×10^{-29}	[67]
α	1.35	1.43	[67]
Equivalent lattice parameter a	2.85×10^{-10}	2.85×10^{-10}	This work

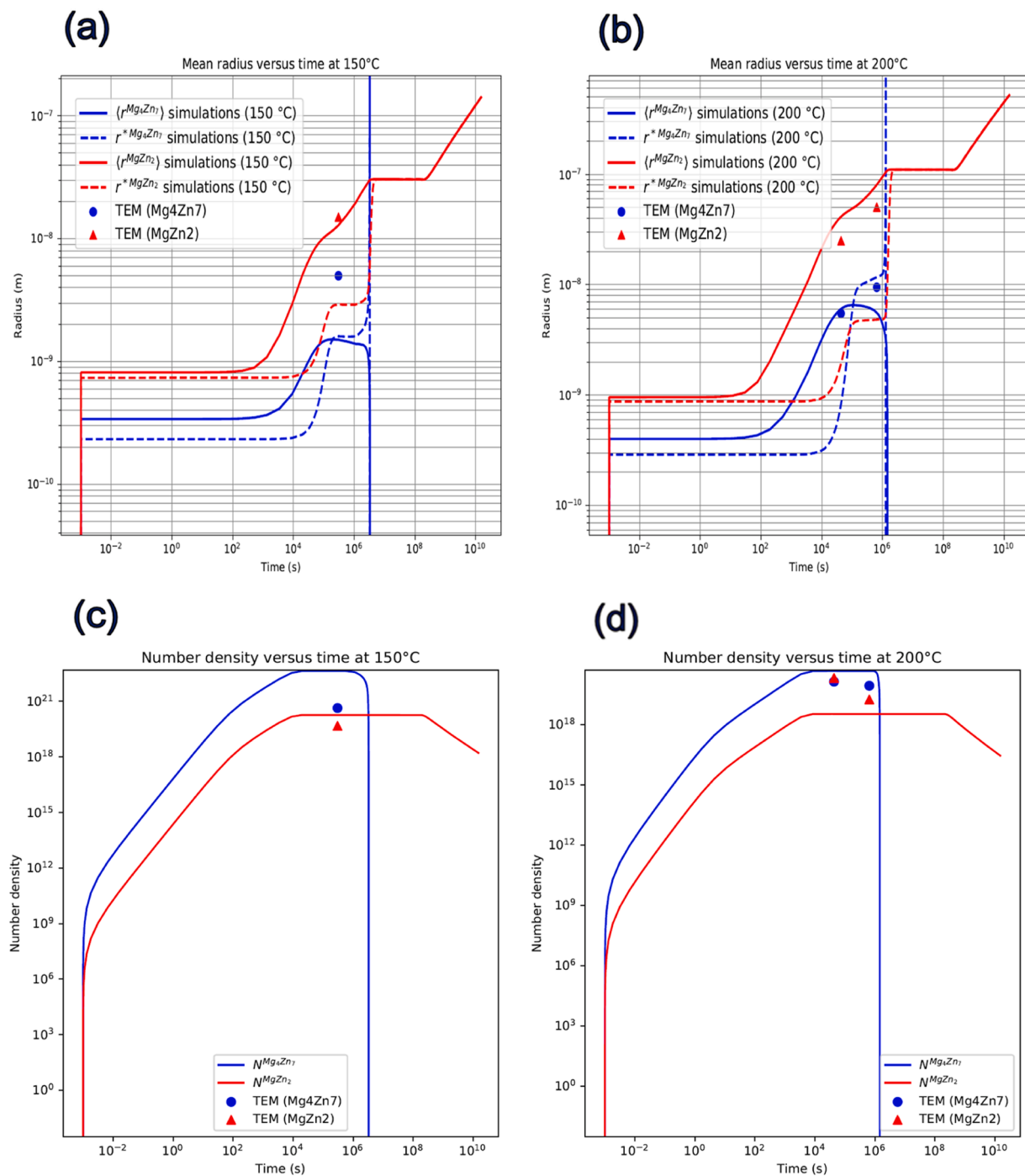


Fig. 10. Simulation results of (a)(b) mean radius and (c)(d) number density evolution of rod (Mg_4Zn_7) and plate-shaped (MgZn_2) precipitates in Mg-1.7at.%Zn alloy during aging at (a)(c) 150 °C and (b)(d) 200 °C, in comparison with experimental data from TEM.

Although this might be true for the long aging time where the precipitates are largely incoherent, some influence of the precipitates might arise at the early aging time where the precipitates are smaller with added coherency. Such influences have been reported in some other alloying systems. For example, in a TEP study of Al-Mg-Si alloy, the prevalence of a semi-coherent phase causes an increase in TEP signal [74], it is believed to be due to the evolution in the intrinsic effect of the precipitates during the phase transformation [75–77]. The misfitting precipitates are also shown to induce the change in matrix lattice parameters in the XRD studies on Cu, Al alloys and steel [78,79]. While a slight change of lattice parameters could lead to a considerable variation of solute content during the XRD analysis, according to Fig. 7. However,

the intrinsic influence from precipitates on TEP and XRD analysis differs from material to material. Quantifying this influence in the current system is challenging.

Regarding the APT and TEM, they provide direct and precise microstructural and chemical information. However, these techniques are only able to analyze relatively small volumes, and the extrapolation of these results to the bulk can be hindered by the presence of local inhomogeneity in the material, as was revealed earlier in SEM observations in Fig. 4. The TEM results are also affected by the significant errors arising from the estimation of the foil thickness to obtain the precipitates volume fractions. In the current study, an uncertainty of $\sim 10\%$ was observed between the foil thicknesses measured from EELS and

CBED. Also, when using TEM to access the solute content, other errors could come from the assumptions of precipitate composition when translating the volume fraction into solute concentration.

5.2. Evolution of precipitate volume fraction during aging

The solute content obtained in Fig. 8 can be translated to precipitate volume fraction using a variation of Eq. (10), with the exception of TEM where precipitate volume fraction was first obtained, assuming a certain composition for all precipitates:

$$f_v = \frac{X_{Zn}^0 - X_{Zn}}{\alpha (X_{Zn}^0 - X_{Zn})} \quad (30)$$

For the case of the β_2 plate, the stoichiometry of $MgZn_2$ is well-established. There is, however, some uncertainty regarding the composition of the β_1 precipitates. Up to now, the proposed compositions for β_1 rod found in the literature are meta-stable Mg_4Zn_7 [23–26] and $MgZn_2$ [21,22]. They have even been found to coexist as dual phases in a single β_1 rod [27]. The question is to what degree the variation from one composition to another could affect the calculation of precipitate volume fraction. To answer this, the translated volume fractions of precipitates using Eq. (30) at 150 °C and 200 °C from different techniques (except TEM, which is a direct measurement) are depicted in Fig. 11 to have a direct comparison. Note that, in each translated result, all precipitates can only be assumed to have one composition, in this case, either Mg_4Zn_7 or $MgZn_2$. Respectively solid points and hollow points from TEP represent the translated volume fraction assuming all precipitates have the composition of Mg_4Zn_7 ($FV_{Mg_4Zn_7}$) and $MgZn_2$ (FV_{MgZn_2}). The difference between $FV_{Mg_4Zn_7}$ (solid points) and FV_{MgZn_2} (hollow points) at the early aging stage appears negligible. For a longer aging time, the difference becomes more significant with average $FV_{Mg_4Zn_7}$ is ~ 10% higher than FV_{MgZn_2} . Overall, the difference is small. Recent simulation works based on first principle methods indicate that hexagonal $MgZn_2$ is more thermally stable than monoclinic Mg_4Zn_7 , but they have similar formation energies [80,81]. It is likely that the composition of the β_1 rods evolves from the metastable Mg_4Zn_7 at early aging times to the more stable $MgZn_2$ for longer aging times. Hence the “real” volume fraction will be closer to $V_{Mg_4Zn_7}$ during the early aging and tend towards FV_{MgZn_2} at the later aging stage (from both β_1 rods and β_2 plates, with the dominant composition of $MgZn_2$). This agrees with the volume fraction measured in TEM on an over-aged sample, which is

closer to FV_{MgZn_2} .

5.3. Modeling precipitate volume fraction

The precipitate volume fraction can be computed from calculated radius and number densities. Historically $MgZn_2$ has been used as the only phase in existing models for the β_1 rods [59,60], which has the limitation of not accounting for the possible presence of β_2 plates. Since changing precipitate composition does not induce a significant variation of estimated volume fraction, and for the convenience of distinguishing two precipitate species, the simulation in this work uses Mg_4Zn_7 to represent β_1 rods and $MgZn_2$ to represent β_2 plates.

Fig. 12 gives the simulated Zn solute concentration and precipitate volume fraction in comparison with the experimental results. It shows that the Zn concentration evolution measured experimentally is pretty well captured by the model (Fig. 12 (a) and (b)). Note that there is a small plateau in the simulated curve which indicates the transition from one composition to the other. Fig. 12 (c) and (d) show the competition of volume fraction kinetics between β_1 rods and β_2 plates. Before peak aging, β_1 rods dominate the precipitation, and are then gradually replaced by β_2 plates. This is a new finding that has not been previously shown in the literature [59,60]. The simulated results for the β_2 plates agree well with the TEM measurements and tend towards FV_{MgZn_2} in Fig. 11. The simulated results for the β_1 rods are below the $FV_{Mg_4Zn_7}$ in Fig. 11 but above the XRD and TEM results. This is reasonable as the experiments measure the overall precipitate volume fraction of Mg_4Zn_7 and $MgZn_2$, while the simulated β_1 rods only consider the composition of Mg_4Zn_7 .

Based on the above information, a TTT (time-temperature-transformation) diagram can be calculated and proposed for the meta-stable $MgZn_2$ and Mg_4Zn_7 phases in the Mg-1.7at.%Zn alloy (Fig. 13), where the time and temperatures required to reach 20%, 50% and 80% of maximum volume fraction of each phase are presented. Both phases show typical C-shape curves, with the Mg_4Zn_7 phase forming first and the two phases starting to overlap at higher temperatures. This study is the first report of such a TTT diagram for the Mg-Zn system.

Although the present work considers both β_1 and β_2 with certain compositions (Mg_4Zn_7 and more stable $MgZn_2$), these precipitates would display a range of intermediate compositions which are not accounted for in the current model. The assumptions on precipitate

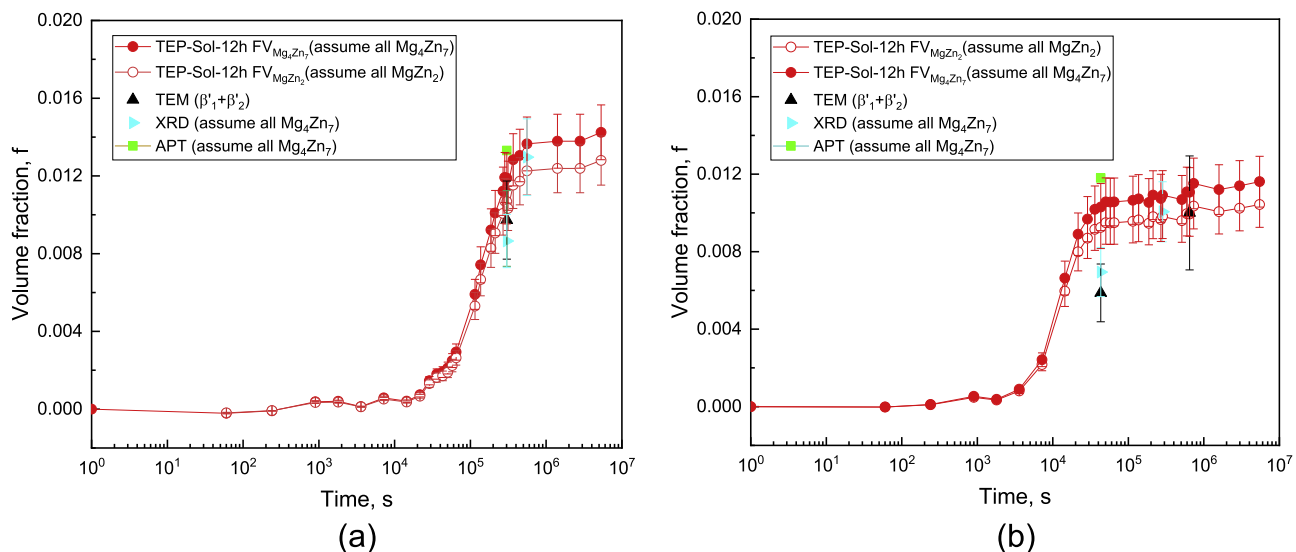


Fig. 11. Precipitate volume fraction evolution as a function of aging time obtained from different characterization techniques at (a) 150 °C and (b) 200 °C. Solid points consider all precipitates are Mg_4Zn_7 (except TEM), hollow points consider all precipitates are $MgZn_2$.

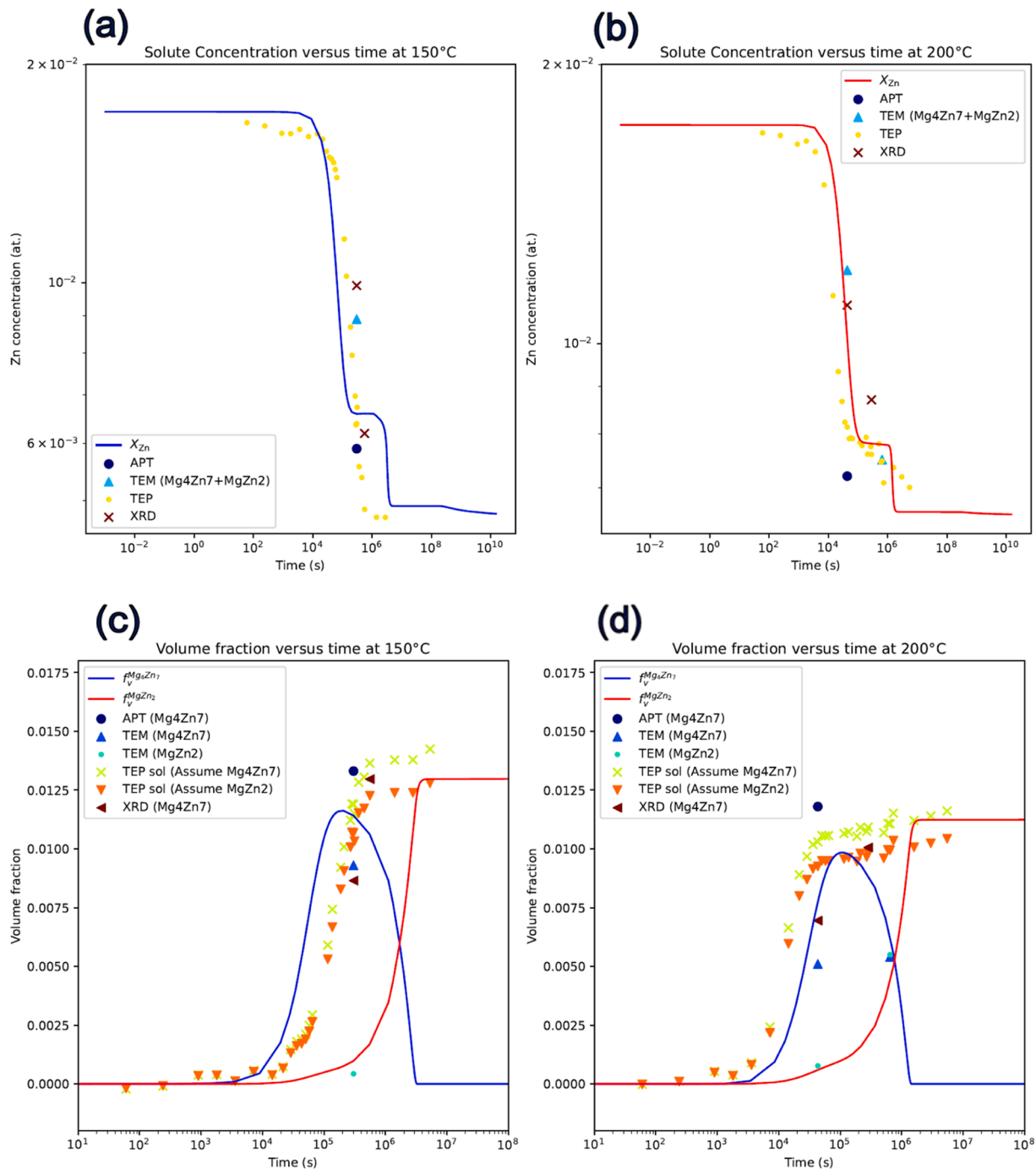


Fig. 12. Simulation results of (a)(b) Zn solute concentration and (c)(d) volume fraction evolution of rod and plate-shaped precipitates in Mg-1.7at.%Zn alloy during aging at (a)(c) 150 °C and (b)(d) 200 °C, in comparison with experimental data.

compositions can explain some of the discrepancies between the model and experimental results. One of the key assumptions to obtain the solubility product was that the microstructures are fully precipitated, which is likely not the case leading to a slight underestimation of the total volume of precipitates at equilibrium. However, our current study only focuses on the meta-stable phases, and the final equilibrium state is not considered. Overall, the proposed model, combined with the experimental results, assists in better understanding the precipitation sequence in Mg-Zn alloys.

6. Conclusion

The current study used multiple characterization techniques and a precipitation model to provide new perspectives in understanding complex precipitation in Mg-Zn alloys. The main conclusions are summarized below:

- A combination of different techniques is used to measure the size of precipitates and solute concentration in Mg-Zn alloy; the precipitation kinetics is well characterized. TEP was applied in Mg alloy to follow the precipitation kinetics for the first time.

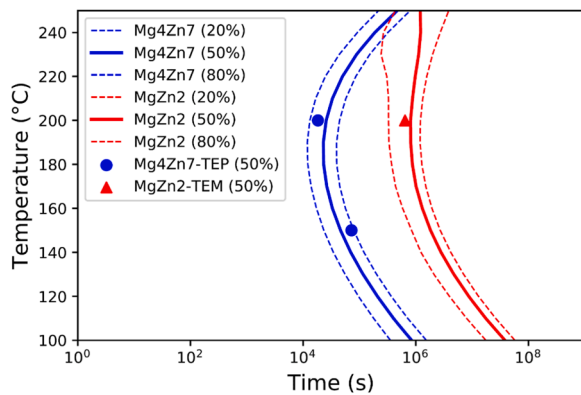


Fig. 13. TTT diagram of the formation of Mg_4Zn_7 and $MgZn_2$ phases in Mg-1.7at.%Zn alloy. Experimental data estimated from TEP and TEM are also shown.

- Solubility limit from this study at 150 °C and 200 °C was found to be lower than that predicted by the current phase diagram in database (THERMOCALC, PANDAT and KNOVEL).
- A precipitation model based on classical nucleation and coarsening theories was adapted for Mg-Zn alloys, and it was likely to reproduce microstructural evolutions of β_1' and β_2' precipitates in Mg-Zn Alloy. A TTT diagram is proposed for this system.
- Experimental and simulation results show that β_1' dominates the precipitation at the early aging stage, while β_2' starts to form after ~ 84 h at 150 °C and ~ 12 h at 200 °C and prevails for the longer aging time.

Declaration of Competing Interest

The authors declare that they have no known competing financial interests or personal relationships that could have appeared to influence the work reported in this paper.

Acknowledgements

The authors thank the Deakin Advanced Characterization Facility and Australian Synchrotron, part of ANSTO, for supporting the characterization work and experimental beamtime at the Powder Diffraction beamline. Fundings provided by Australian Research Council Discovery Grant (DP150101577) and China Scholarship Council (201706370176) are also acknowledged. Yi Yang would like to acknowledge MATEIS team in INSA Lyon for their technical and financial support under the Nicolas Baudin Travel Grant Scheme.

Reference

- [1] A. Ardell, Precipitation hardening, *Metallurgical Transactions A* 16 (12) (1985) 2131–2165.
- [2] J.D. Robson, N. Stanford, M.R. Barnett, Effect of precipitate shape on slip and twinning in magnesium alloys, *Acta materialia* 59 (5) (2011) 1945–1956.
- [3] J. Clark, L. Zabdyr, Z. Moser, Phase diagrams of binary magnesium alloys, ASM International, Materials Park, OH, 1988, pp. 353–364.
- [4] M. Easton, A. Beer, M. Barnett, C. Davies, G. Dunlop, Y. Durandet, S. Blacket, T. Hilditch, P.J.J. Beggs, Magnesium alloy applications in automotive structures 60 (11) (2008) 57.
- [5] J. Hirsch, T. Al-Samman, Superior light metals by texture engineering: Optimized aluminum and magnesium alloys for automotive applications, *Acta Materialia* 61 (3) (2013) 818–843.
- [6] W.J. Joost, P.E. Krajewski, Towards magnesium alloys for high-volume automotive applications, *Scripta Materialia* 128 (2017) 107–112.
- [7] S. Zhang, X. Zhang, C. Zhao, J. Li, Y. Song, C. Xie, H. Tao, Y. Zhang, Y. He, Y. Jiang, Y. Bian, Research on an Mg–Zn alloy as a degradable biomaterial, *Acta Biomaterialia* 6 (2) (2010) 626–640.
- [8] J. Clark, Transmission electron microscopy study of age hardening in a Mg-5 wt.% Zn alloy, *Acta Metallurgica* 13 (12) (1965) 1281–1289.

- [9] J. Buha, Reduced temperature (22–100°C) aging of an Mg–Zn alloy, *Materials Science & Engineering: A* 492 (1–2) (2008) 11–19.
- [10] J. Buha, The effect of micro-alloying addition of Cr on age hardening of an Mg–Zn alloy, *Materials Science & Engineering: A* 492 (1–2) (2008) 293–299.
- [11] J. Buha, The effect of Ba on the microstructure and age hardening of an Mg–Zn alloy, *Materials Science & Engineering: A* 491 (1–2) (2008) 70–79.
- [12] I. Polmear, *Light alloys: from traditional alloys to nanocrystals*, Elsevier, 2005.
- [13] I. Polmear, Magnesium alloys and applications, *Materials Science & technology* 10 (1) (1994) 1–16.
- [14] J.F. Nie, Precipitation and hardening in magnesium alloys, *Metallurgical and Materials Transactions A* 43 (2012) 3891–3939.
- [15] N. Stanford, M. Barnett, Effect of particles on the formation of deformation twins in a magnesium-based alloy, *Materials Science and Engineering: A* 516 (1–2) (2009) 226–234.
- [16] J. Wang, N. Stanford, Investigation of precipitate hardening of slip and twinning in Mg5% Zn by micropillar compression, *Acta Materialia* 100 (2015) 53–63.
- [17] J. Jain, P. Cizek, W. Poole, M. Barnett, Precipitate characteristics and their effect on the prismatic-slip-dominated deformation behaviour of an Mg–6 Zn alloy, *Acta materialia* 61 (11) (2013) 4091–4102.
- [18] J. Wang, M.R.G. Ferdowsi, S.R. Kada, P.A. Lynch, Z. Wang, J.A. Kimpton, M. R. Barnett, Stress relaxations during cyclic loading-unloading in precipitation hardened Mg-4.5 Zn, *Acta Materialia* 205 (2021), 116531.
- [19] J. Wang, M.R.G. Ferdowsi, P.A. Lynch, S.R. Kada, M.R. Barnett, Influence of precipitation on tension and compression twinning in Mg-6.5 Zn alloy, *Scripta Materialia* 207 (2022), 114253.
- [20] J.F. Nie, Effects of precipitate shape and orientation on dispersion strengthening in magnesium alloys, *Scripta Materialia* 48 (8) (2003) 1009–1015.
- [21] L. Wei, G. Dunlop, H. Westengen, Precipitation hardening of Mg-Zn and Mg-Zn-RE alloys, *Metallurgical Materials Transactions A* 26 (7) (1995) 1705–1716.
- [22] J. Gallot, R. Graf, Nouvelles observations aux rayons x et au microscope électronique sur la phase transitoire appraisant dans l'alliage magnésium-zinc 6 (de zinc), *Comptes rendus hebdomadaires des seances de l'academie des sciences* 261 (3) (1965) 728. -&.
- [23] X. Gao, J.F. Nie, Characterization of strengthening precipitate phases in a Mg–Zn alloy, *Scripta Materialia* 56 (8) (2007) 645–648.
- [24] A. Singh, A. Tsai, Structural characteristics of β_1' precipitates in Mg–Zn-based alloys, *Scripta Materialia* 57 (10) (2007) 941–944.
- [25] A. Singh, J.M. Rosalie, H. Somekawa, T. Mukai, The structure of precipitates in Mg–Zn–Y alloys, *Philosophical Magazine Letters* 90 (9) (2010) 641–651.
- [26] J.M. Rosalie, H. Somekawa, A. Singh, T. Mukai, Structural relationships among $MgZn_2$ and Mg_4Zn_7 phases and transition structures in Mg–Zn–Y alloys, *Philosophical Magazine* 90 (24) (2010) 3355–3374.
- [27] J.M. Rosalie, H. Somekawa, A. Singh, T. Mukai, Orientation relationships between icosahedral clusters in hexagonal $MgZn_2$ and monoclinic Mg_4Zn_7 phases in Mg–Zn (–Y) alloys, *Philosophical Magazine* 91 (19–21) (2011) 2634–2644.
- [28] M. Karlik, A. Bigot, B. Joffrey, P. Auger, S. Belliot, HREM, FIM and tomographic atom probe investigation of Guinier–Preston zones in an Al–1.54 at% Cu alloy, *Ultramicroscopy* 98 (2–4) (2004) 219–230.
- [29] K.E. Knippling, R.A. Karnesky, C.P. Lee, D.C. Dunand, D.N. Seidman, Precipitation evolution in Al–0.1 Sc, Al–0.1 Zr and Al–0.1 Sc–0.1 Zr (at.%) alloys during isochronal aging, *Acta Materialia* 58 (15) (2010) 5184–5195.
- [30] J.M. Rosalie, H. Somekawa, A. Singh, T. Mukai, The effect of size and distribution of rod-shaped β_1' precipitates on the strength and ductility of a Mg–Zn alloy, *Materials Science & Engineering: A* 539 (2012) 230–237.
- [31] J.M. Rosalie, H. Somekawa, A. Singh, T. Mukai, Effect of precipitation on strength and ductility in a Mg–Zn–Y alloy, *Journal of alloys & compounds* 550 (2013) 114–123.
- [32] J.M. Rosalie, B.R. Pauw, Form-free size distributions from complementary stereological TEM/SAXS on precipitates in a Mg–Zn alloy, *Acta materialia* 66 (2014) 150–162.
- [33] N. Mo, I. McCarroll, Q. Tan, A. Ceguerra, Y. Liu, J. Cairney, H. Dieringa, Y. Huang, B. Jiang, F. Pan, Understanding solid solution strengthening at elevated temperatures in a creep-resistant Mg–Gd–Ca alloy, *Acta Materialia* 181 (2019) 185–199.
- [34] D.H. Ping, K. Hono, J.F. Nie, Atom probe characterization of plate-like precipitates in a Mg–RE–Zn–Zr casting alloy, *Scripta Materialia* 48 (8) (2003) 1017–1022.
- [35] T. Honma, T. Ohkubo, K. Hono, S. Kamado, Chemistry of nanoscale precipitates in Mg–2.1 Gd–0.6 Y–0.2 Zr (at.%) alloy investigated by the atom probe technique, *Materials Science & Engineering: A* 395 (1–2) (2005) 301–306.
- [36] K. Oh-Ishi, C. Mendis, T. Ohkubo, K. Hono, Effect of laser power and specimen temperature on atom probe analyzes of magnesium alloys, *Ultramicroscopy* 111 (6) (2011) 715–718.
- [37] M. Perez, F. Perrard, V. Massardier, X. Kleber, A. Deschamps, H. De Monestrol, P. Pareige, G. Covarel, Low-temperature solubility of copper in iron: experimental study using thermoelectric power, small angle X-ray scattering and tomographic atom probe, *Philosophical Magazine* 85 (20) (2005) 2197–2210.
- [38] M. Perez, V. Massardier, X. Kleber, Thermoelectric power applied to metallurgy: principle and recent applications, *International journal of materials research* 100 (10) (2009) 1461–1465.
- [39] J. Pelletier, G. Vigier, J. Merlin, P. Merle, F. Fouquet, R. Borrelly, Precipitation effects on thermopower in Al–Cu alloys, *Acta Metallurgica* 32 (7) (1984) 1069–1078.
- [40] G. Raynaud, P. Guyot, Coherent precipitation effect on thermo-power of Al–Cu alloys, *Acta Metallurgica* 36 (1) (1988) 143–147.
- [41] W. Pearson, Lattice spacings and structures of metals and alloys, Vols. I & II (1958).

- [42] Á. Filep, M. Sepsi, Determination of solid solution composition in Al alloys by electrical transport properties measurement and XRD method, in: IOP Conference Series: Materials Science and Engineering, IOP Publishing, 2018.
- [43] R. Wagner, R. Kampmann, P.W. Voorhees, Homogeneous second-phase precipitation, *Phase transformations in materials* (2001) 309–407.
- [44] M. Perez, M. Dumont, D. Acevedo-Reyes, Implementation of classical nucleation and growth theories for precipitation, *Acta materialia* 56 (9) (2008) 2119–2132.
- [45] M. Perez, M. Dumont, D. Acevedo-Reyes, Corrigendum to “Implementation of classical nucleation and growth theories for precipitation” [*Acta Materialia* 56 (2008) 2119–2132], *Acta Materialia* 57 (2009) 1318. -1318.
- [46] A. Graux, S. Cazottes, D. De Castro, D. San Martín, C. Capdevila, J.M. Cabrera, S. Molas, S. Schreiber, D. Mirković, F. Danoix, Precipitation and grain growth modeling in Ti-Nb microalloyed steels, *Materialia* 5 (2019), 100233.
- [47] O. Myhr, Ø. Grong, Mode of the age hardening behaviour of Mg of non-isothermal transformations in alloys containing a particle distribution, *Acta Materialia* 48 (7) (2000) 1605–1615.
- [48] O. Myhr, Ø. Grong, S. Andersen, Modeling of the age hardening behaviour of Al-Mg-Si alloys, *Acta Materialia* 49 (1) (2001) 65–75.
- [49] M. Nicolas, A. Deschamps, Characterisation and modeling of precipitate evolution in an Al-Zn-Mg alloy during non-isothermal heat treatments, *Acta Materialia* 51 (20) (2003) 6077–6094.
- [50] S. Samaras, Modeling of microstructure evolution during precipitation processes: a population balance approach of the KWN model, *Modelling & Simulation in Materials Science & Engineering* 14 (8) (2006) 1271.
- [51] A. Eivani, H. Ahmed, J. Zhou, J. Duszczak, An experimental and theoretical investigation of the formation of Zr-containing dispersoids in Al-4.5 Zn-1Mg aluminum alloy, *Materials Science & Engineering: A* 527 (9) (2010) 2418–2430.
- [52] J. Robson, Modeling competitive continuous and discontinuous precipitation, *Acta Materialia* 61 (20) (2013) 7781–7790.
- [53] D. Bardel, M. Perez, D. Nelias, A. Deschamps, C.R. Hutchinson, D. Maisonnette, T. Chaise, J. Garnier, F. Bourlier, Coupled precipitation and yield strength modeling for non-isothermal treatments of a 6061 aluminium alloy, *Acta Materialia* 62 (2014) 129–140.
- [54] R. Chen, Q. Xu, B. Liu, Modeling investigation of precipitation kinetics and strengthening for needle/rod-shaped precipitates in Al-Mg-Si alloys, *Acta Metall Sin* 52 (8) (2016) 987–999.
- [55] B. Holmedal, E. Osmundsen, Q. Du, Precipitation of non-spherical particles in aluminum alloys part I: generalization of the Kampmann-Wagner numerical model, *Metallurgical and Materials Transactions A* 47 (2016) 581–588.
- [56] Q. Du, B. Holmedal, J. Friis, C.D. Marioara, Precipitation of non-spherical particles in aluminum alloys Part II: numerical simulation and experimental characterization during aging treatment of an Al-Mg-Si alloy, *Metallurgical and Materials Transactions A* 47 (2016) 589–599.
- [57] Y. Li, B. Holmedal, H. Li, L. Zhuang, J. Zhang, Q. Du, Precipitation and strengthening modeling for disk-shaped particles in aluminum alloys: Size distribution considered, *Materialia* 4 (2018) 431–443.
- [58] J. Miao, C. Zhang, A.D. Klarner, J. Zhang, E. Cinkilic, F. Zhang, A.A. Luo, Characterization and modeling of concurrent precipitation in Mg-Al-Sn alloys using an improved Kampmann-Wagner numerical (KWN) model, *Materialia* 21 (2022), 101348.
- [59] J. Robson, C. Paa-Rai, The interaction of grain refinement and aging in magnesium-zinc-zirconium (ZK) alloys, *Acta Materialia* 95 (2015) 10–19.
- [60] M. Paliwal, I.-H. Jung, Precipitation kinetic model and its applications to Mg alloys, *Calphad* 64 (2019) 196–204.
- [61] v.L. Nordheim, C. Gorter, Bemerkungen über thermokraft und widerstand, *Physica* 2 (1935) 383–390.
- [62] K.S. Wallwork, B.J. Kennedy, D. Wang, The high resolution powder diffraction beamline for the Australian Synchrotron, in: AIP Conference Proceedings, American Institute of Physics, 2007.
- [63] J.S. Evans, *Advanced input files & parametric quantitative analysis using topas*. in *Materials Science Forum*, Trans Tech Publ, 2010.
- [64] A. Handbook, *Metallography and Microstructures*, 9, ASM International. Chemical and Electrolytic Polishing, 2004, pp. 281–293.
- [65] J. Wang, M.R.G. Ferdowsi, S.R. Kada, S. Babaniaris, B. Hutchinson, P.A. Lynch, M. R. Barnett, Appearance of textures with a c-axis parallel to the extrusion direction in Mg alloys, *Scripta Materialia* 210 (2022), 114422.
- [66] C.L. Mendis, C.J. Bettles, M. Gibson, C. Hutchinson, An enhanced age hardening response in Mg-Sn based alloys containing Zn, *Materials Science & Engineering: A* 435 (2006) 163–171.
- [67] K. Momma, F. Izumi, VESTA 3 for three-dimensional visualization of crystal, volumetric and morphology data, *Journal of applied crystallography* 44 (6) (2011) 1272–1276.
- [68] B. Smith, knovel: Engineering & Scientific Online References, Reference Reviews (2002).
- [69] J.O. Andersson, T. Helander, L. Höglund, P.f. Shi, B. Sundman, Thermo-Calc & DICTRA, computational tools for materials science, *Calphad* 26 (2) (2002) 273–312.
- [70] S.-L. Chen, S. Daniel, F. Zhang, Y. Chang, X.-Y. Yan, F.-Y. Xie, R. Schmid-Fetzer, W. Oates, The PANDAT software package and its applications, *Calphad* 26 (2) (2002) 175–188.
- [71] A. Balan, M. Perez, T. Chaise, S. Cazottes, D. Bardel, F. Corpace, F. Pichot, A. Deschamps, F. De Geuser, D. Nelias, Precipitation of γ in Inconel 718 alloy from microstructure to mechanical properties, *Materialia* 20 (2021), 101187.
- [72] M. Perez, Gibbs-Thomson effects in phase transformations, *Scripta materialia* 52 (8) (2005) 709–712.
- [73] C. Kammerer, N.S. Kulkarni, R.J. Warmack, Y.H. Sohn, Interdiffusion and impurity diffusion in polycrystalline Mg solid solution with Al or Zn, *Journal of alloys & compounds* 617 (2014) 968–974.
- [74] G. Meyruey, V. Massardier, W. Lefebvre, M. Perez, Over-aging of an Al-Mg-Si alloy with silicon excess, *Materials Science & Engineering: A* 730 (2018) 92–105.
- [75] D. Dafir, Etude de l'influence du renfort sur la cinétique de précipitation dans un composite 6061/SiCp élaboré par métallurgie des poudres, INSA, Lyon, 1993.
- [76] D. Eskin, V. Massardier, P. Merle, A study of high-temperature precipitation in Al-Mg-Si alloys with an excess of silicon, *Journal of materials science* 34 (1999) 811–820.
- [77] V. Massardier, T. Epicier, P. Merle, Correlation between the microstructural evolution of a 6061 aluminium alloy and the evolution of its thermoelectric power, *Acta materialia* 48 (11) (2000) 2911–2924.
- [78] M. Akhlaghi, T. Steiner, S.R. Meka, A. Leineweber, E.J. Mittemeijer, Lattice-parameter change induced by accommodation of precipitate/matrix misfit; misfitting nitrides in ferrite, *Acta Materialia* 98 (2015) 254–262.
- [79] M. Akhlaghi, T. Steiner, S.R. Meka, E.J. Mittemeijer, Misfit-induced changes of lattice parameters in two-phase systems: coherent/incoherent precipitates in a matrix, *Journal of Applied Crystallography* 49 (1) (2016) 69–77.
- [80] Y.P. Xie, Z.Y. Wang, Z.F. Hou, The phase stability and elastic properties of MgZn₂ and Mg₄Zn₇ in Mg-Zn alloys, *Scripta Materialia* 68 (7) (2013) 495–498.
- [81] X.D. Li, H.T. Ma, Z.H. Dai, Y.C. Qian, L.J. Hu, Y.P. Xie, First-principles study of coherent interfaces of Laves-phase MgZn₂ and stability of thin MgZn₂ layers in Mg-Zn alloys, *Journal of Alloys & Compounds* 696 (2017) 109–117.